Global and regional patterns of soil nitrous acid emissions and their acceleration of rural photochemical reactions

Dianming Wu[1,2,†,*], Jingwei Zhang[3,4,†], Mengdi Wang[1,2,†], Junling An[3,4,*], Ruhai Wang[5], Haroon Haider[1,2], Xu-Ri[6,7], Ye Huang[1,2], Qiang Zhang[8,9], Feng Zhou[10], Hanqin Tian[11], Xiuying Zhang[12], Lingling Deng[1,2], Yuepeng Pan[3], Xi Chen[1], Yuanchun Yu[13], Chunsheng Hu[14], Rui Wang[1,2], Yaqi Song[1,13], Zhiwei Gao[1,2], Yue Wang[1,2], Lijun Hou[15], Min Liu[1,2,*]

[1]Key Laboratory of Geographic Information Science (Ministry of Education), School of Geographic Sciences, East China Normal University, Shanghai, China.
[2]Institute of Eco-Chongming (IEC), Shanghai, China.
[3]State Key Laboratory of Atmospheric Boundary Layer Physics and Atmospheric Chemistry (LAPC), Institute of Atmospheric Physics (IAP), Chinese Academy of Sciences, Beijing, China.
[4]College of Earth and Planetary Sciences, University of Chinese Academy of Sciences, Beijing, China.
[5]State Key Laboratory of Soil and Sustainable Agriculture, Institute of soil Sciences, Chinese Academy of Sciences, Nanjing, China.
[6]Key Laboratory of Alpine Ecology and Biodiversity, Institute of Tibetan Plateau Research, Chinese Academy of Sciences, Beijing, China.
[7]CAS Center for Excellence in Tibetan Plateau Earth Sciences, Beijing, China.
[8]Ministry of Education Key Laboratory for Earth System Modeling, Department of Earth System Science, Tsinghua University, Beijing, China.
[9]Collaborative Innovation Center for Regional Environmental Quality, Beijing, China.
[10]Sino-France Institute of Earth Systems Science, Laboratory for Earth Surface Processes, College of Urban and Environmental Sciences, Peking University, Beijing, China.
[11]International Center for Climate and Global Change Research and School of Forestry and Wildlife Sciences, Auburn University, Auburn, USA.
[12]International Institute for Earth System Science, Nanjing University, Nanjing, China.
[13]Co-Innovation Center for the Sustainable Forestry in Southern China, College of Biology and the Environment, Nanjing Forestry University, Nanjing, China.
[14]Key Laboratory of Agricultural Water Research, Center for Agricultural Resources Research, Institute of Genetic and Developmental Biology, Chinese Academy of Sciences, Shijiazhuang, China.
[15]State Key Laboratory of Estuarine and Coastal Research, East China Normal University, Shanghai, China.

Corresponding author: Dianming Wu (dmwu@geo.ecnu.edu.cn); Junling An (anjl@mail.iap.ac.cn); Min Liu (mliu@geo.ecnu.edu.cn)

† Dianming Wu, Jingwei Zhang, and Mengdi Wang contributed equally to this work.

Key Points:

- The best estimate of global soil HONO emissions in 2017 is 9.67 with a range of 7.36-11.99 Tg N yr^{-1}, where cropland soils accounted for ~ 79%.
- Soil HONO emissions enhanced ground OH concentrations by 10-60% and ozone concentrations by 0.5-1.5 ppb at daytime.
- The impact of soil HONO emissions on OH budgets were more important in rural than urban areas.

Abstract

Abiotic and biotic releases of nitrous acid (HONO) from soils contribute substantially to the missing source of tropospheric HONO and hydroxyl radicals (OH). However, global and regional patterns of soil HONO emissions are rarely quantified, and the contributions of such emissions to atmospheric oxidization capacity are unclear. Here, we present that the best estimate of global soil HONO emissions in 2017 is 9.67 with a range of 7.36-11.99 Tg N yr^{-1}, where cropland soils accounted for ~ 79%. The analyses also indicate that regional soil HONO emissions enhanced ground OH concentrations by 10-60% and ozone concentrations by 0.5-1.5 ppb at daytime in the ambient area of Shanghai, China. The impact of soil HONO emissions on OH budgets were more important in rural than urban areas. These findings suggest that the global soil HONO emissions, especially from cropland, could quicken photochemical reactions and aggravate air pollution in rural areas.

1 Introduction

Reactive nitrogen (N_r) gases released from the land surface strongly affect the Earth's atmosphere through atmospheric cycling of hydroxyl radicals (OH) and ozone (O_3) (Crutzen, 1970; Elshorbany et al., 2012; Liang et al., 1998; Pinder et al., 2012). While soil emissions of nitrous acid (HONO) have been recently reported (Oswald et al., 2013; Su et al., 2011; Wu et al., 2019), the associated global patterns and impacts on air quality are poorly defined. Lacking data on global and regional soil HONO emissions and accurate assessments of atmospheric oxidation capacity limit our understanding of atmospheric HONO sources and sinks, OH recycling, the formation of secondary aerosols and O_3, and biogeochemical N cycling.

Soil HONO emissions were studied to explain the unknown daytime atmospheric HONO sources in many regions, such as Meusel et al. (2018) and Sörgel et al. (2015). The proposed underlying mechanisms include chemical equilibrium with soil nitrite (NO_2^-) (Su et al., 2011), microbiological nitrification or denitrification pathways (Oswald et al., 2013; Wu et al., 2019), soil mineral surface acidification caused by amphoteric metal oxides or nitrate accumulation (Donaldson et al., 2014; Kim & Or, 2019), and acid displacement (VandenBoer et al., 2015). Moreover, the emission rates of soil HONO are comparable to those of nitric oxide (NO) measured in laboratory (Oswald et al., 2013; Weber et al., 2015). Soil NO emissions have been widely studied globally and regionally by both bottom-up and top-down models (Bertram et al., 2005; Ganzeveld et al., 2002; Yienger & Levy II, 1995). The IPCC (Ciais et al., 2013) and other studies (Hudman et al., 2012; Miyazaki et al., 2017; Steinkamp & Lawrence, 2011; Vinken et al., 2014; Yan et al., 2005; Yienger & Levy II, 1995) reported a broad range of global soil nitrogen oxide [NO_x = NO + nitrogen dioxide (NO_2)] emissions of 4.7-16.8 Tg yr^{-1} (in terms of nitrogen, hereinafter referred to as Tg N yr^{-1}). The large uncertainties might be caused by specific parameters, including emissions factors, land cover maps, the impact of precipitation on NO_x emissions assumed in semi-empirical models, and the uncertain relationship between observed NO_2 concentrations and soil NO_x emissions using the Ozone Monitoring Instrument (OMI) model (Rasool et al., 2019; Steinkamp & Lawrence, 2011).

However, the estimation of soil HONO emissions is rare either at the global or regional scale due to a lack of data and appropriate method. Wu et al. (2019) estimated that global soil HONO emissions at high moisture ranged from 0.03-0.20 Tg N yr^{-1}, while the estimated global

HONO emissions from biological soil crusts in drylands were approximately 0.6 ± 0.1 Tg N yr^{-1} (Weber et al., 2015). A process-oriented representation of soil N emissions in the Community Multiscale Air Quality model (CMAQ) was developed to simulate soil HONO emissions based on the proportions of HONO relative to total NO_x in the United States (Rasool et al., 2019). The monthly average emission rates of soil NO and HONO were highest in fertilized agricultural regions with large spatial and temporal heterogeneity (Rasool et al., 2019). An estimation of global natural and cropland soil HONO emissions has not been reported.

Atmospheric HONO sources are not well understood, and the default HONO formation mechanism (NO+OH→HONO) always severely underestimates HONO observations and atmospheric oxidation capacity as a result. Several potential HONO sources (traffic emissions, NO_2 heterogeneous reactions, etc.) have been coupled into regional chemical transport models (e.g., the Weather Research and Forecasting model with Chemistry (WRF-Chem) and CMAQ). The results showed that potential HONO sources could significantly enhance atmospheric oxidation capacity and lead to increases in the concentrations of fine particulate matter ($PM_{2.5}$), O_3, and secondary organic aerosols (SOA) (Li et al., 2010; Zhang et al., 2019; Zhang et al., 2016). Although soil HONO emissions have been included in the chemical transport model in recent years (Wang et al., 2021; Zhang et al., 2019; Zhang et al., 2016), large uncertainties in soil HONO emissions remain.

Here, we compiled a dataset of global soil samples related to HONO emissions and estimated global soil HONO emissions with a resolution of 0.1° × 0.1° using an empirical "wetting-drying" model. Soil NO and NO_x emissions were also calculated to verify the method accuracy by comparison with reported values. A statistical model was also used to calculate global soil HONO emissions. The simulations of global and regional chemical transport models are similar, but it is very difficult to evaluate the global model performance in terms of simulated HONO values due to extremely limited global HONO observations in the same period. Thus, we used the regional WRF-Chem model to quantify the impacts of local soil HONO emissions on the concentrations of atmospheric HONO, OH and O_3 in Shanghai, China, and its surrounding areas. The model may perform well elsewhere too for future related studies. Comprehensive measurements of soil HONO flux were conducted in this study, and abundant environmental/meteorological observations were collected for model validation.

2 Materials and Methods

2.1 Soil samples

We compiled a dataset of global soil sample data published in different studies related to soil HONO emissions (S11-S21, S33-S44, S55-S64, and S67-S78; see Figure S1 and Table S1). Parts of soil physicochemical properties were collected from cited references, while other soil properties were derived from different sources. Soil inorganic nitrogen (NH_4^+, NO_2^-, and NO_3^-) contents were obtained from Xu-Ri & Prentice (2008), pH, TC, TOC, and TN values were downloaded from the Global Soil Dataset for use in Earth System Models (GSDE) (Shangguan et al., 2014), and soil texture data (clay, silt, and sand) were obtained from the Harmonized World Soil Database (HWSD) v 1.2. We used data from these soil samples together with soil

samples from Shanghai, China (see details in the following information), to estimate global and regional soil emissions of HONO.

We took 35 soil samples (S1-S10, S22-S32, S45-S54, S65, S66, S77, and S78) from different land cover types of Shanghai during July 2018. The sampling sites are located in eastern China (120°52'E-122°12'E, 30°40'N-31°53'N) with a typical subtropical humid monsoon climate. The mean annual temperature, precipitation and sunshine hours were 17.7 ℃, 1388.8 mm and 1809.2 h, respectively, in 2017. All of the samples were taken from the upper layer of the soil (0-5 cm). Each sample was separated into two parts: one part was stored at -20 ℃ and used to measure soil water content, particle size distribution and inorganic nitrogen; the other part was air-dried at room temperature (~ 25 ℃), sieved to 2 mm for measuring soil pH and soil HONO, NO, and NO_x flux, and sieved to 0.15 mm for measuring soil TN and TC. Figure S1 and Table S1 provide more detailed information about the soils.

Soil pH was measured using a glass electrode (FE28, Mettler-Toledo) after shaking a soil and water suspension at a ratio of 1:2.5 (weight/volume, w/v) for 30 min. Soil water content was calculated through the drying method (105 °C, 24 h). Inorganic nitrogen was extracted with 2 mol L^{-1} potassium chloride (KCl, 1:2.5 w/v) and then determined by a continuous flow analyser (Skalar San++ System, Skalar). Soil TC, TOC and TN were measured by a TOC-L analyser (TOC-L, Shimadzu). Soil particle size was analysed using a laser diffraction particle size analyser (LA-960A, HORIBA).

2.2 HONO, NO, and NO_x flux measurements

Soil N_r gas flux was measured with a dynamic chamber system, which has been described in detail elsewhere (Wu et al., 2019). Previous studies showed that this technique can well simulate reactive gas flux from field measurements (Plake et al., 2015; Rummel et al., 2002; van Dijk et al., 2002). Briefly, 40 grams of air-dried soil was put into a petri dish (inner diameter = 94 mm) and wetted with purified water to the water holding capacity (WHC, %). Then, the petri dish was placed into a Teflon chamber (volume ~ 10 L) with a fan coated with Teflon to mix the gases inside the chamber. Purified air without water and reactive gases (such as HONO, NO_x, O_3, and C_xH_y) were flushed into the chamber with a flow rate of 6 L min^{-1}. Thus, the wetted soil in the chamber was dried during measurements, which was defined as a full wetting-drying cycle when no water vapor was detected in the chamber. The mixing ratio of HONO in the headspace was determined by high-performance liquid chromatography (HPLC, Agilent 1200, Agilent Technologies) based on the derivatization of nitrite with sulfanilamide (SA) and N-(1-naphthyl)-ethylenediamine dihydrochloride (NED) under acidic conditions (Huang et al., 2002; Wu et al., 2020). The time resolution was ~ 6 min, and the lower detection limit was ~ 4 ppt for HONO. The mixing ratios of NO and NO_2, CO_2, and H_2O in the headspace were determined by a NO_x chemiluminescence analyzer (Model 42iTL, Thermo Scientific), an ozone analyser (Model 49i, Thermo Scientific), and a LI-COR (Model 840A, LI-COR), respectively. Due to the overestimation by the chemiluminescence analyzer, NO_2 data were corrected by multiplying by 0.6, which was from the relationship of measured NO_2 concentrations between the chemiluminescence analyzer and an improved incoherent broadband cavity-enhanced absorption spectroscopy (IBBCEAS) system (Tang et al., 2020). All of the experiments were

conducted at a constant temperature of 25 ℃ in the dark. The fluxes of HONO, NO, and NO_x were calculated using equation 1:

$$F = \frac{Q * M_N}{A * V_m} * X \quad (1)$$

where F is the flux of reactive nitrogen gas (ng N m^{-2} s^{-1}). Q is the chamber air flow rate (m^3 s^{-1}). M_N is the molar mass of nitrogen (g mol^{-1}). A is the area of the soil surface (m^2). V_m is the molar volume under standard reference atmospheric conditions (m^3 mol^{-1}). X is the headspace concentration of N_r gas (ppb).

2.3 Integrated soil N_r gas emissions per wetting-drying cycle

Integrated emissions of HONO, NO, and NO_x from Shanghai soils during a full wetting-drying cycle were calculated according to equation 2:

$$E_{N,int} = \sum_{i=0}^{i=max} F_i * (t_i - t_{i-1}) * 10^{-6} \quad (2)$$

where $E_{N,int}$ is the integrated emission of N_r gas (mg N m^{-2}). t_i is the measurement time for i. F_i is the flux of N_r gas at t_i (ng N m^{-2} s^{-1}). Supplementary Text S1 and Figure S2 show more information about the results.

We also collected data on integrated soil HONO, NO, and NO_x emissions from various ecosystems (see Supplementary Text S1, Table S1 and Figure S2). Then, we calculated the integrated emissions of HONO, NO, and NO_x from different land cover types per wetting-drying cycle ($E_{N,int,LC}$, mg N m^{-2}; average ± standard error) (for specific values, see Supplementary Text S1). The land cover types (LC), including cropland (CR), forest (FR), grassland (GL), shrubland (SL), wetland (WL), and bare land (BL), were classified according to Gong et al. (2019). Natural vegetation (NV) was defined as all of the land cover types except cropland. We adjusted the spatial resolution of the land cover map to 0.1° × 0.1° to be consistent with the precipitation data.

2.4 Upscaling soil emissions of N_r gases to global scale

We estimated global soil HONO, NO, and NO_x emissions based on the empirical "wetting-drying method" as described by Weber et al. (2015), which showed consistent results with those estimated by a process-based modelling approach (Porada et al., 2019).

First, the N_r emissions per grid cell containing different land cover types induced by precipitation and temperature ($E_{LC,cell}$, kg N ha^{-1} yr^{-1}) could be obtained according to equation 3:

$$E_{\mathrm{LC,cell}} = E_{\mathrm{N,int,LC}} * P_{\mathrm{cell}} * T_{\mathrm{cal}} * 10^{-2} \quad (3)$$

where P_{cell} represents the number of precipitation events for each grid cell during one year; one precipitation event was defined by a daily rainfall at the central point > 0.1 mm. The one-day multi-satellite precipitation data were obtained from NASA and had a spatial resolution of 0.1° × 0.1° (Huffman et al., 2019). T_{cal} represents the calibration factor of temperature (Hudman et al., 2012), which can be calculated by the following equation 4:

$$T_{\mathrm{cal}} = e^{0.103*T}/(Q_{10} * 2.5) \quad (4)$$

where T is monthly averaged soil surface (0-7 cm) temperature (℃) from the datasets of ERA5-Land (Muñoz Sabater, 2019), Q_{10} is temperature coefficient (Winkler et al., 1996) and the value is calculated and averaged based on soil flux of HONO, NO, and NO_x at different

temperature from the data of Wu et al. (2019) and Oswald et al. (2013). 2.5 is the calibrated constant of soil temperature.

Then, the fertilizer-induced direct emissions from cropland per grid cell ($E_{\text{fer,cell}}$, kg N ha^{-1} yr^{-1}) were added using the emission factor method according to equation 5:

$$E_{\text{fer,cell}} = F_{\text{cell}} * EF * 10^{-2} \quad (5)$$

where F_{cell} is the amount of fertilizer input in different grid cells (kg N ha^{-1} yr^{-1}) and was obtained from the National Bureau of Statistics of China (2018) and the Food and Agriculture Organization of the United Nations (FAO, 2017). *EF* is the emission factor (%) induced by fertilization. The value of the *EF*s were described in details in Text S2.

Soil HONO, NO, and NO_x emissions from different land cover types caused by precipitation and fertilization ($E_{\text{LC,Nr}}$ and $E_{\text{fer,Nr}}$, Tg N yr^{-1}) were calculated according to equations 6 and 7:

$$E_{\text{LC,Nr}} = \sum_{i=1}^{n} E_{\text{LC,cell}} * A * 10^{-9} \quad (6)$$

$$E_{\text{fer,Nr}} = \sum_{j=1}^{m} E_{\text{fer,cell}} * A * 10^{-9} \quad (7)$$

where *i* is the number of grid cells of different land cover types and *j* is the number of grid cells of cropland. A is a constant representing the area of each grid cell (~ 12,321 hectares).

Finally, we calculated the global or regional soil HONO, NO, and NO_x emissions ($E_{\text{GR, Nr}}$, Tg N yr^{-1}) above plant canopy using equation 8:

$$E_{\text{GR,Nr}} = \left(E_{\text{CR,Nr}} + E_{\text{FR,Nr}} + E_{\text{GL,Nr}} + E_{\text{SL,Nr}} + E_{\text{WL,Nr}} + E_{\text{BL,Nr}} + E_{\text{fer,Nr}}\right) * CRF \quad (8)$$

where $E_{\text{GR,Nr}}$ represents the global soil N_r emissions $E_{\text{global,Nr}}$ or different regional soil N_r emissions $E_{\text{regional,Nr}}$ (see Table 1). *CRF* represents the canopy reduction factor, which can be calculated using equation 9:

$$CRF = \left(\frac{e^{-(k_S * SAI)} + e^{-(k_C * LAI)}}{2}\right) \quad (9)$$

where k_s and k_c are absorptivity constants of plant leaves and set as 8.75 and 0.24 m^2 m^{-2} (Yienger & Levy II, 1995). *LAI* represents leaf area index, which is obtained from the database of NOAA Global Inventory Monitoring and Modeling System (GIMMS) (Zhu et al., 2013). *SAI* represents stomatal area index, which is calculated based on the value of *LAI*/*SAI* under different land cove types (Yienger & Levy II, 1995). The ranges of global and regional soil HONO, NO, and NO_x emissions were calculated based on the minimum and maximum values of $E_{\text{N,int,LC}}$ (see Supplementary Text S1).

2.5 Impacts of soil HONO emissions on air quality

The soil HONO emissions of the 35 soil samples from Shanghai and the improved WRF-Chem model 3.7.1 were used to evaluate the impact of soil HONO emissions on atmospheric HONO, OH and O_3 concentrations. Two domains were adopted in this study: domain 1 covered eastern China and contained 71×71 grid cells with a horizontal resolution of 27 km, and domain 2 covered Shanghai and its surrounding regions and contained 45×45 grid cells with a horizontal resolution of 9 km. Shanghai is located in the center of domain 2; the blue dot is the HONO observation site, the 8 black dots (urban) and 1 red dot (rural) are the O_3 and NO_2 observation sites, and the 26 purple dots are meteorological sites. Detailed locations of the 36 sites are given

in Table S2. The physical and chemical options in the WRF-Chem model used in this study are given in Table S3.

A previous study showed a strong positive correlation (r = 0.93) between field soil HONO flux and solar radiation and found that the fluxes were quite small at nighttime and strongest at noontime (Xue et al., 2019). Thus, we revised the soil HONO flux measured by the dynamic chamber system based on this relationship (see equation 10) and inserted it into our model.

$$F_{(\mathrm{RHONO,LC})} = \frac{SR}{IA} * E_{\mathrm{N,int}} * 10^6 * \frac{1}{3600} \quad (10)$$

where $F_{(\mathrm{RHONO,LC})}$ represents the revised soil HONO flux (ng N m^{-2} s^{-1}) for a certain land cover type (including cropland, forest, grassland, and urban green land), *SR* denotes the direct solar radiation intensity (W m^{-2}), *IA* represents the integrated energy per area during daytime (W h m^{-2}), and $E_{\mathrm{N,int}}$ is the integrated soil HONO emissions (mg N m^{-2}) per wetting-drying process.

Equation 10 was established under three assumptions: (1) the integrated soil HONO emissions during the wetting-drying period were the optimum amount; (2) a typical soil wetting-drying period lasted for one day after rainfall; and (3) the optimum amount of soil HONO emissions was only reached on sunny days with the strongest solar radiation (noontime radiation intensity of ~ 900 W m^{-2}, integrated energy of ~ 6000 W h m^{-2}, and daytime radiant energy of ~ 2.16×10^7 J m^{-2}). For cloudy days with weaker solar radiation, the emissions were reduced according to the radiant energy ratio; i.e., a daytime radiant energy of 1.08×10^7 J m^{-2} corresponded to 50% of the maximum amount for a cloudy day with a wetting-drying process.

In total, 10 cases were conducted in this study, i.e., base, soil-A, soil-B, soil-C, 5S-A, 5S-B, 5S-C, base-low, soil-low, and 5S-low cases. The base case only considered the gas-phase production of HONO (NO+OH→HONO). The soil-A case added averaged soil HONO emissions. The 5S-A case added 5 potential HONO sources (5S), including traffic HONO emissions, biomass burning emissions, NO_2 heterogeneous reactions on aerosol and ground surfaces, and average soil HONO emissions. The other 7 cases were designed to evaluate the uncertainties of soil HONO emissions and the effects of anthropogenic NO_x emissions on atmospheric oxidation capacity and O_3 concentrations. A detailed description and parameterizations can be found in our previous work (Zhang et al., 2019) and Tables S4 and S5.

Due to the lack of atmospheric HONO observations during the period of soil sampling in Shanghai, another set of field HONO observations in Shanghai reported by Bernard et al. (2016) was collected to evaluate the model performance in terms of HONO simulation. The HONO observations were collected from October 16-24, 2009. Thus, we conducted the base and 5S-A cases focusing on general HONO simulations in the period of October 16-24, 2009, and all 10 cases focused on soil HONO emissions in the period of March 2016. Our results showed that the five potential HONO sources could significantly improve HONO simulations and reasonably reproduce observations (Figure S3). The simulated and observed meteorological factors and NO_2/O_3 concentrations were also comparable (see more details in Supplementary Text S3, Figures S4 and S5, and Table S6).

Two anthropogenic emission inventories were adopted in this study. The MIX (2010) inventory from Li et al. (2017) was used for the simulations in 2009. The MEIC inventory from Li et al. (2017) and updated to 2016 was used for the simulations in 2016. The horizontal

resolutions of the two inventories were 0.5° and 0.25°, respectively. Detailed information on the inventories can be found in our previous work (Zhang et al., 2019).

3 Results and Discussions

3.1 Global and regional patterns of soil HONO emissions using an empirical "wetting-drying" model

The best estimate of global soil emissions of HONO above plant canopy in 2017 was 9.67 (minimum-maximum estimates: 7.36-11.99) Tg N yr^{-1}, consisting of 7.65 (6.30-9.01) and 2.02 (1.06-2.97) Tg N yr^{-1} from cropland and natural vegetation, respectively (Table 1). Asia was the largest contributor (average estimate: 4.70 Tg N yr^{-1}) among the continents, accounting for ~ 49% of global soil HONO emissions, followed by Africa (2.02 Tg N yr^{-1}), South America (1.32 Tg N yr^{-1}), North America (0.83 Tg N yr^{-1}), Europe (0.52 Tg N yr^{-1}), and Oceania (0.23 Tg N yr^{-1}) (Table 1). Figure 1a shows the global spatial distribution of soil HONO emissions above canopy. The global average soil emissions of HONO were 0.64 (0.49-0.80) kg N ha^{-1} yr^{-1}. The hotspot areas of soil emissions of HONO were mainly from croplands, including in the South and East Asia, the middle of North and South America and Africa, and Europe.

Table 1. Global and regional soil emissions of HONO, NO, and NO_x (E_{HONO}, E_{NO}, and E_{NOx}) above plant canopy.

Regions	**Sources**	**Above canopy emissions (Tg N yr^{-1})**		
		E_{HONO}	E_{NO}	E_{NOx}
Global	Cropland	7.65 (6.30-9.01)[a]	9.42 (7.68-12.18)	12.03 (10.42-13.64)
	Natural vegetation	2.02 (1.06-2.97)	4.35 (2.32-6.39)	7.11 (2.86-11.36)
	Total	9.67 (7.36-11.99)	13.78 (9.99-18.57)	19.14 (13.28-25.00)
Africa	Cropland	1.56 (1.28-1.83)	1.78 (1.47-2.09)	2.11 (1.79-2.44)
	Natural vegetation	0.47 (0.27-0.67)	1.37 (0.88-1.86)	2.10 (1.07-3.13)
	Total	2.02 (1.55-2.50)	3.15 (2.36-3.95)	4.22 (2.86-5.57)
North America	Cropland	0.60 (0.49-0.72)	0.78 (0.66-0.91)	1.01 (0.87-1.14)
	Natural vegetation	0.23 (0.12-0.34)	0.43 (0.21-0.65)	0.71 (0.28-1.14)
	Total	0.83 (0.61-1.06)	1.21 (0.87-1.55)	1.71 (1.15-2.28)
South America	Cropland	0.70 (0.57-0.83)	0.87 (0.73-1.02)	1.07 (0.92-1.23)
	Natural vegetation	0.62 (0.31-0.94)	1.13 (0.55-1.70)	1.82 (0.67-2.96)
	Total	1.32 (0.88-1.77)	2.00 (1.28-2.72)	2.89 (1.59-4.19)
Asia	Cropland	4.24 (3.50-4.98)	5.32 (4.26-7.39)	6.99 (6.11-7.87)
	Natural vegetation	0.46 (0.23-0.68)	0.83 (0.33-1.33)	1.49 (0.41-2.58)
	Total	4.70 (3.73-5.66)	6.15 (4.59-8.72)	8.48 (6.52-10.45)
Europe	Cropland	0.44 (0.36-0.52)	0.56 (0.47-0.65)	0.72 (0.62-0.81)
	Natural vegetation	0.09 (0.04-0.13)	0.15 (0.07-0.23)	0.24 (0.09-0.40)
	Total	0.52 (0.40-0.65)	0.71 (0.54-0.87)	0.96 (0.71-1.21)
Oceania	Cropland	0.08 (0.07-0.10)	0.10 (0.09-0.12)	0.13 (0.11-0.15)
	Natural vegetation	0.15 (0.09-0.21)	0.45 (0.26-0.63)	0.74 (0.34-1.15)
	Total	0.23 (0.16-0.31)	0.55 (0.35-0.75)	0.87 (0.45-1.30)
China	Cropland	0.52 (0.44-0.61)	0.64 (0.55-0.74)	0.88 (0.78-0.98)
	Natural vegetation	0.06 (0.03-0.09)	0.09 (0.04-0.15)	0.16 (0.04-0.28)

	Total	0.58 (0.46-0.70)	0.74 (0.59-0.89)	1.04 (0.82-1.26)
East China	Cropland	0.44 (0.37-0.51)	0.54 (0.46-0.63)	0.75 (0.66-0.83)
	Natural vegetation	0.04 (0.02-0.07)	0.07 (0.02-0.11)	0.11 (0.03-0.20)
	Total	0.49 (0.39-0.58)	0.61 (0.49-0.73)	0.86 (0.68-1.03)

303 [a]Values are averages with their ranges.

304

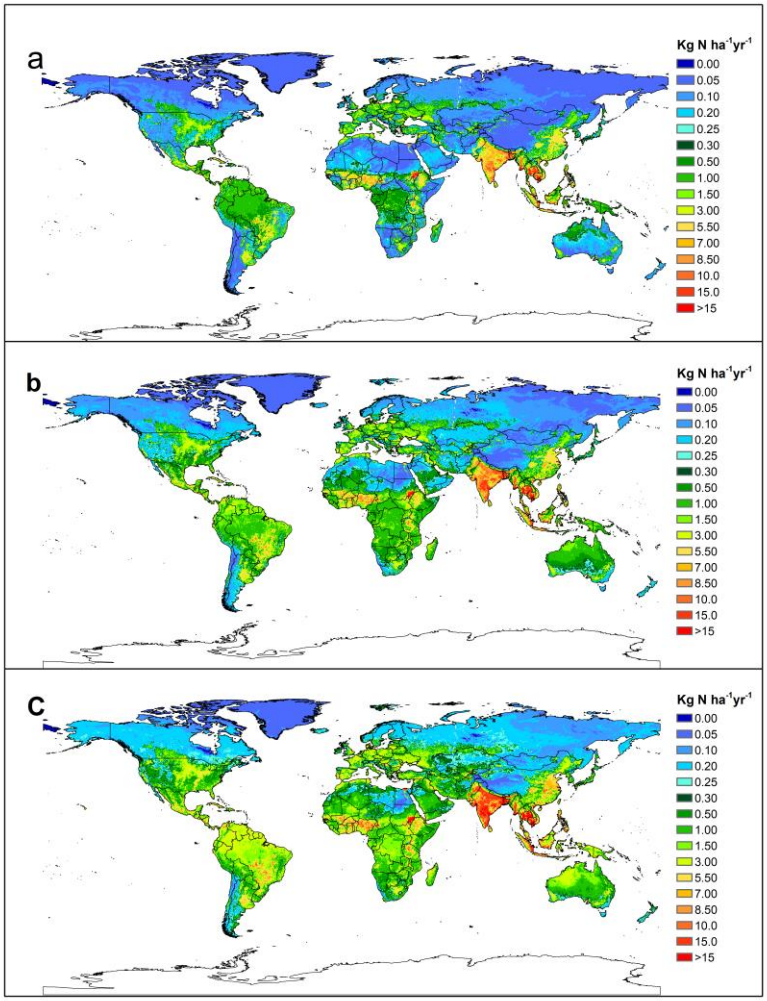

305 **Figure 1**. Global spatial distribution of soil emissions of reactive nitrogen gases (HONO, NO,
306 and NO_x) above canopy. a, HONO. b, NO. c, NO_x. The emissions induced by precipitation and
307 fertilization were estimated by an empirical "wetting-drying" method. The figure was created by
308 Kriging interpolation.

309

310 Previous estimations based on the bottom-up ("wetting-drying") approach used in this
311 study showed global emissions of HONO and NO from biological soil crusts of 0.6 and 1.1 Tg N
312 yr^{-1} (Weber et al., 2015), which was consistent with the estimations by a process-based model
313 (0.69 and 1.04 Tg N yr^{-1}) (Porada et al., 2019). We also compared our data with the reported

values in previous studies. In general, the estimated soil HONO flux was in the range of reported surface flux measured either in field or laboratory, and also might explain the unknown daytime HONO source (Table S7). Rasool et al. (2019) showed that soil NO+HONO emissions from the eastern United States were in the range of 0–30 ng N m^{-2} s^{-1}, while our calculation was 0–53 ng N m^{-2} s^{-1} (Figure 1). Ren et al. (2011) reported an average HONO flux of -0.056 ± 3.36 ng N m^{-2} s^{-1} above forest canopy by using the relaxed eddy accumulation method, while our calculation was 0.095 ng N m^{-2} s^{-1}. Laufs et al. (2017) reported that daytime HONO flux above an agricultural crop field was in the range of 0.1 to 2.3 ng N m^{-2} s^{-1}, while our estimated soil HONO flux was approximately 2.63 ng N m^{-2} s^{-1} in the same location. Ramsay et al. (2018) reported the HONO flux above an agricultural grassland was in the range of -2.46 to 4.92 ng N m^{-2} s^{-1}, with the maximum achieved after fertilization, while our estimation was 0.92 ng N m^{-2} s^{-1}. The maximum soil HONO flux can even be more than 1000 ng N m^{-2} s^{-1} after fertilization in agricultural field (Tang et al., 2019; Xue et al., 2019). The average agricultural soil HONO flux was in the range of -0.86 to 20.25 ng N m^{-2} s^{-1} measured by field dynamic chambers (Tang et al., 2019), while our estimated value was approximately 8.53 ng N m^{-2} yr^{-1} in the same location. We also compared the soil emissions of NO and NO_x with the reported values, and the results showed good agreement (see more details in Supplementary Text S4).

3.2 Global soil emissions of HONO using a statistical model related to edaphic factors

Soil HONO emissions are controlled by (de)nitrification and other nitrogen cycling processes and are thus affected by soil edaphic factors (Donaldson et al., 2014; Kim & Or, 2019; Maljanen et al., 2013; Oswald et al., 2013; Scharko et al., 2015; Su et al., 2011; Wu et al., 2019). Here, we found that the maximum soil HONO flux ($F_{HONO,max}$) during a wetting-drying cycle was significantly correlated with soil pH, the ratio of total carbon (TC) to total nitrogen (TN), the ratio of nitrite nitrogen (NO_2^--N) to ammonium nitrogen (NH_4^+-N), NO_2^--N, sand, and silt content at a global scale (Tables S1 and S8). For HONO emissions from local (Shanghai) soils measured in this study, the controlling factors were more related to soil nitrate nitrogen (NO_3^--N), NO_2^--N, the ratio of total organic carbon (TOC) to NO_3^--N, and NO_3^--N/NH_4^+-N (Tables S1 and S8). Although Homyak et al. (2015) found unbuffered KCl extractions underestimated NO_2^--N concentration in acidic soil, most of the soil samples in our measurements were alkaline or neutral, and thus it should not affect our results. Furthermore, soil NO_3^--N rather than NO_2^--N content was used in the statistical model, indicating that our conclusions would not be affected.

Thus, we established a statistical model to simulate soil HONO emissions ($F_{HONO,model}$) using the above soil edaphic factors and water content (SWC), expressed as equations 11 and 12 (see more details in Supplementary Text S5 and Figure S6). This model could accurately predict soil HONO emissions with changes in SWC (Figure S7) and might potentially be applied in the prediction of global seasonal changes in soil HONO emissions. The estimated global soil HONO emissions based on this statistical model were 13.37 (9.29-17.12) Tg N yr^{-1}, with 5.79 (3.84-7.74) Tg N yr^{-1} from cropland (Table 2). This method had much higher emissions from bare land 5.23 (4.17-5.98) Tg N yr^{-1} than did the "wetting-drying" model 0.26 (0.17-0.35) Tg N yr^{-1}. The reason could be due to higher HONO emissions at lower soil moisture for bare land (global average approximately 15% WHC) than other land cover soils (global average approximately 30-50% WHC) (Figures S6 and S7). The statistical method also had higher emissions from grassland and wetland than did the "wetting-drying" model, while it had lower emissions from cropland and forest. Nevertheless, the estimated global soil HONO emissions were close to each

other, 8.14 and 9.41 Tg N yr^{-1} for the statistical and "wetting-drying" method, respectively, if bare land was not included.

$$\boldsymbol{F_{HONO,model} = (0.02 + 0.77 * 0.99^{(f(SWC)-f(swc,max))^2}) * F_{LC,HONO,max}} \quad (11)$$

$$\boldsymbol{f(SWC,max) = -5.97 * x_1 + 2.99 * x_2 - 0.02 * x_3 + 53.76} \quad (12)$$

where f(SWC) (%) represents the SWC corresponding to the normalized soil HONO flux (the ratio of soil HONO flux to $F_{HONO,max}$); f(SWC,max) (%) represents the simulated SWC corresponding to $F_{HONO,max}$; $F_{LC,HONO,max}$ (ng N m^{-2} s^{-1}) represents the average $F_{HONO,max}$ from different land cover types; and x_1, x_2, and x_3 represent soil pH, TOC (%), and NO_3^--N (mg kg^{-1}) content, respectively.

Table 2. Comparisons of global soil HONO emissions above canopy from cropland, forest, grassland, shrubland, wetland, and bare land calculated by the empirical "wetting-drying" method and statistical model.

Land cover	HONO (Tg N yr^{-1})	
	Empirical "wetting-drying" method	Statistical model
Bare land	0.26 (0.17-0.35)[a]	5.23 (4.17-5.98)
Cropland	7.65 (6.30-9.01)	5.79 (3.84-7.74)
Forest	1.12 (0.48-1.76)	0.76 (0.43-1.08)
Grassland	0.60 (0.39-0.81)	1.29 (0.70-1.87)
Shrubland	0.01 [b]	0.11[b]
Wetland	0.02 (0.01-0.04)	0.20 (0.05-0.34)
Total	9.67 (7.36-11.99)	13.37 (9.29-17.12)

[a]Values are averages with their ranges.

[b]Due to lacking data, the ranges are not available in here.

3.3 Soil HONO emissions enhanced atmospheric oxidation capacity

Based on the WRF-Chem simulations, soil HONO emissions played a more important role in daytime atmospheric HONO concentrations in rural (~20–50%) than urban areas (< 10%, Figure 2). The reasons could be attributed to the larger soil HONO emission rates and smaller contributions from other potential HONO sources in rural areas, where traffic emissions and NO_2 heterogeneous reactions were both weaker with lower NO_x concentrations (Finlayson-Pitts et al., 2003). Soil HONO emissions mainly enhanced atmospheric HONO and OH concentrations near the ground, while the enhancements were limited above 500 m (Figure 3). For those four soil categories in the study region including cropland, forest, grassland and urban green land, the enhanced daytime HONO concentrations were 0.07 ± 0.02, 0.10 ± 0.06, 0.05 ± 0.03, and 0.03 ± 0.01 ppb near the ground, respectively, while the corresponding OH concentrations were enhanced by 0.61 ± 0.18 × 10^6, 0.66 ± 0.44 × 10^6, 0.54 ± 0.32 × 10^6, and 0.15 ± 0.05 × 10^6 molecules cm^{-3} near the ground, respectively. Due to the weaker termination by NO_2 (NO_2 + OH → HNO_3) with lower NO_2 concentrations, the enhanced OH concentrations by soil HONO emissions (cropland, grassland, and forest) were much larger in rural (30–60%) than those in urban areas (10–20%) (Figures 2 and 3). Detailed information of the impact of soil HONO

emissions on OH sources and sinks could be found in Figures 3 and S11. The daily maximum 8-h (DMA8) O_3 enhancements were generally larger in rural (approximately 1.0 ppb) than those in urban areas (approximately 0.5 ppb), while the largest hourly O_3 enhancements reached 1.0–3.0 ppb in most part of the region (Figures 2 and 3). Zhang et al. (2016) reported a daily average HONO enhancement of > 1.5 ppb and an O_3 enhancement of 2.4–3.6 ppb after coupling cropland soil HONO emissions (over 100 ng N m^{-2} s^{-1}) into the regional chemical transport model in eastern China. Recently, Wang et al. (2021) reported an O_3 enhancements of 5–6 ppb around noontime with implementing approximately 80 ng N m^{-2} s^{-1} of fertilized soil HONO flux into the CMAQ model. These enhancements were comparable with this study if adopting a smaller soil HONO flux.

We also conducted sensitivity simulations by reducing 50% of anthropogenic NO_x emissions, the lower NO_2 concentrations caused less HONO formation via NO_2 heterogeneous reactions and thus increased the contribution of soil HONO emissions to surface HONO concentrations (Figure 2). The spatial patterns of OH enhancements were similar with or without cutting off anthropogenic NO_x emissions, while the DMA8 O_3 enhancements (1.0–1.5 ppb) and the largest hourly O_3 enhancements (2.0–4.0 ppb) were both larger after reducing 50% of anthropogenic NO_x emissions (Figures 2 and 3). Considering the on-going NO_x emission reduction strategy (Zheng et al., 2018) and the concurrent rising O_3 concentrations in China (Li et al., 2019), soil HONO emissions would further increase atmospheric oxidation capacity and O_3 concentrations and play a noticeable role in air quality degradation in the future.

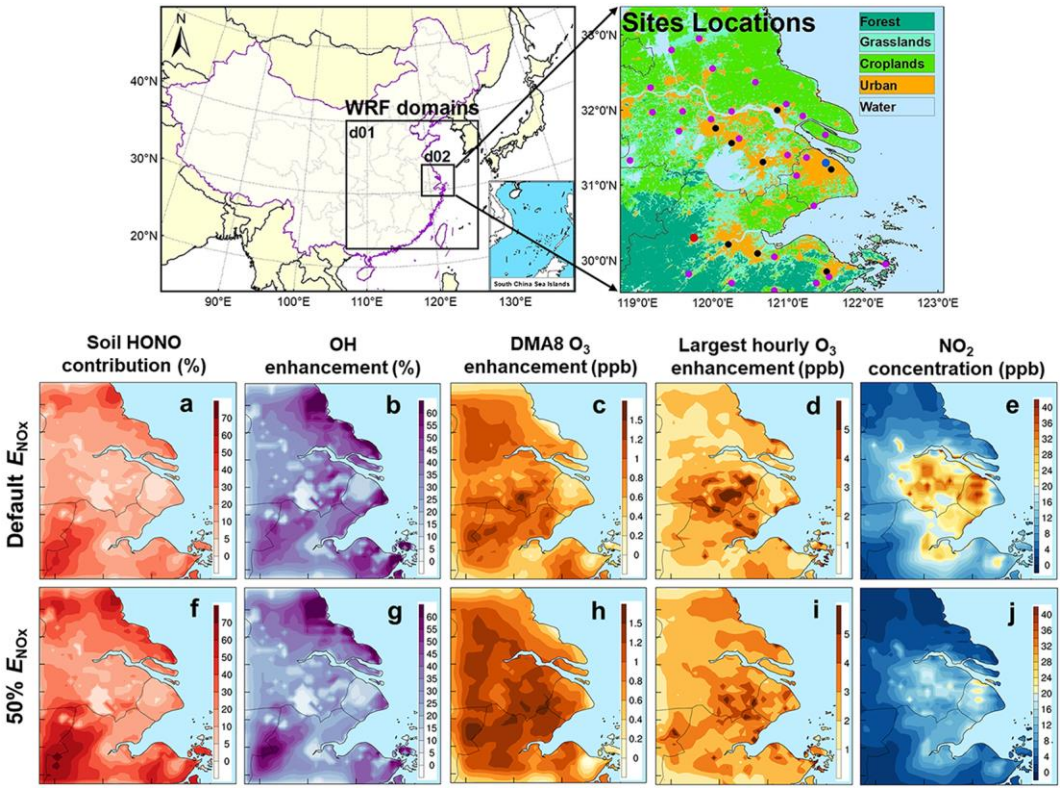

Figure 2. WRF-Chem domains used in this study and the impact of soil HONO emissions on air quality. The used observational sites (blue dot: HONO; black dots: urban NO_2/O_3; red dot: rural NO_2/O_3 at Lin'an; purple dots: meteorology) are shown in the upper panel. The lower panel shows daytime averaged relative contribution of soil HONO emissions to the five potential

HONO sources (a and f), the OH (b and g), the daily maximum 8-h (DMA8) O_3 (c and h) and the largest hourly O_3 (d and i) enhancements compared with the base case, and NO_2 concentrations (e and j) under 100% and 50% NO_x emissions (shown as default and 50% E_{NOx}, respectively) for five typical wetting-drying days in March of 2016.

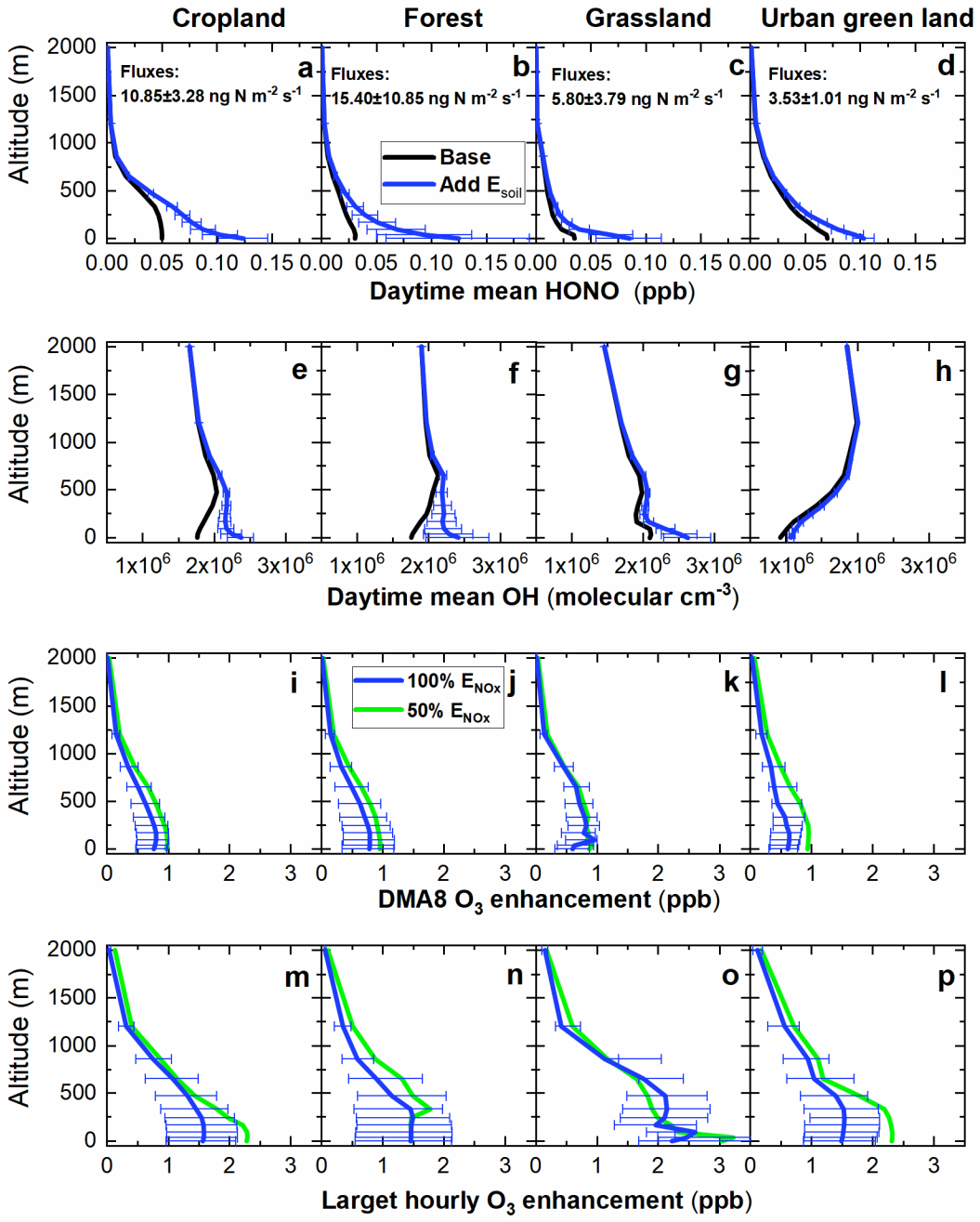

Figure 3. Vertical profiles of simulated HONO and OH concentrations with (cases soil-A, soil-B and soil-C) or without (case base) adding soil HONO emissions (a-f), and the vertical profiles of daily maximum 8-h (DMA8) O_3 enhancement and largest hourly O_3 enhancement induced by

soil HONO emissions (i-p). The blue solid line corresponding to the mean soil HONO emissions, the error bar denotes the impacts of the minimum and maximum soil HONO emissions.

4 Conclusions

We report global soil HONO emissions estimated by two bottom-up methods, an empirical "wetting-drying" model and a statistical model. Both results were constrained by the limited and inconsistent observed data of soil HONO emissions. More field data on soil HONO emissions from different land cover types, especially from bare land and cropland, could improve the accuracy of the model. For the empirical "wetting-drying" method, global precipitation data were derived from multi-satellite rather than ground-observed data, and the fertilization rates of cropland in each country or province were set to the same value according to the FAO (2017), both of these databases had discrepancies with realistic values and could increase uncertainties. Fertilizer-induced soil HONO emissions from global cropland could increase by 1.75 and 0.1 Tg N yr^{-1}, respectively, when applying gridded fertilizer data from Wang et al. (2019) (including synthetic N fertilizer, livestock manure and crop residues applied to cropland) and Lu & Tian (2017) (including synthetic N fertilizer). For the statistical model, global soil HONO emissions were strongly affected by the resolution and accuracy of soil moisture and physicochemical property (pH, TOC, and NO_3^--N) data. If the maximum soil HONO flux corresponding to soil moisture were well constrained, the results of statistical model should be greatly improved.

Soil HONO emissions are controlled by biogeochemical nitrogen cycling, which is affected by nitrogen deposition, temperature, land-use change, and atmospheric carbon dioxide (CO_2) concentrations (Gruber & Galloway, 2008). With climate change and increasing human activities, the land-atmosphere interactions and surface exchange of N_r gases will play more important roles in atmospheric composition and air quality in the future. Based on our simulations, soil HONO emissions accelerated regional HO_x (OH + HO_2) cycling and increased daytime OH concentrations by approximately10–60% and O_3 concentrations by approximately 0.5–1.0 ppb. Considering the stronger soil HONO emissions after fertilization processes (Xue et al., 2021), the impact of soil HONO emissions would be even larger during fertilization periods (Wang et al., 2021). By providing global and regional soil emissions of HONO and the impacts on atmospheric chemistry, our work could potentially help biogeochemical and atmospheric chemistry models constrain global soil N_r emissions and the contribution of soil HONO emissions to atmospheric oxidation capacity.

Acknowledgments

This work was supported by the National Natural Science Foundation of China (41807449, 42077083, 41761144062, 41730646, and 41775161), the Shanghai Pujiang Program (18PJ1403500), the Director's Fund of Key Laboratory of Geographic Information Science (Ministry of Education), East China Normal University (KLGIS2020C01), and the Fundamental Research Funds for the Central Universities (2017-2021).

Data availability Statement

Global fertilizer data for different countries were obtained from FAOSTAT 2019: Fertilizers by Nutrient domain at http://www.fao.org/faostat/en/#data/RFN. Global daily gridded soil moisture and temperature data in 2018 (0.25° × 0.25°, v201706) were downloaded from the Copernicus Climate Change Service (C3S) Climate Data Store (CDS) at https://cds.climate.copernicus.eu/cdsapp#!/dataset/satellite-soil-moisture?tab=overview. Global monthly gridded soil surface (0-7 cm) temperature data in 2018 (0.1° × 0.1°) were downloaded from the Copernicus Climate Change Service (C3S) Climate Data Store (CDS) at https://cds.climate.copernicus.eu/cdsapp#!/search?text=temperature&keywords=((%20%22Variable%20domain:%20Land%20(biosphere)%22%20)%20AND%20(%20%22Spatial%20coverage:%20Global%22%20)). Other data that support the findings of this study are available upon reasonable request from the authors.

References

Bernard F., Cazaunau M., Grosselin B., Zhou B., Zheng J., Liang P., Zhang Y., Ye X., Daële V., Mu Y., Zhang R., Chen J., & Mellouki A. (2016). Measurements of nitrous acid (HONO) in urban area of Shanghai, China. *Environmental Science and Pollution Research*, *23*, 5818-5829. https://doi.org/10.1007/s11356-015-5797-4

Bertram T. H., Heckel A., Richter A., Burrows J. P., & Cohen R. C. (2005). Satellite measurements of daily variations in soil NO_x emissions. *Geophysical Research Letters*, *32*, L24812. https://doi.org/10.1029/2005GL024640

Ciais P., Sabine C., Bala G., Bopp L., Brovkin V., Canadell J., Chhabra A., DeFries R., Galloway J., Heimann M., Jones C., Le Quéré C., Myneni R. B., Piao S., & Thornton P. (2013). Carbon and other biogeochemical cycles. In: Stocker T. F., Qin D., Plattner G.-K., Tignor M., Allen S. K., Boschung J., Nauels A., Xia Y., Bex V., & Midgley P. M., editors. Climate change 2013: the physical science basis. Contribution of Working Group I to the Fifth Assessment Report of the Intergovernmental Panel on Climate Change. Cambridge University Press, Cambridge, United Kingdom and New York, NY, USA, pp. 465-570.

Crutzen P. J. (1970). The influence of nitrogen oxides on the atmospheric ozone content. *Quarterly Journal of the Royal Meteorological Society*, *96*, 320-325. https://doi.org/10.1002/qj.49709640815

Donaldson M. A., Bish D. L., & Raff J. D. (2014). Soil surface acidity plays a determining role in the atmospheric-terrestrial exchange of nitrous acid. *Proceedings of the National Academy of Sciences*, *111*, 18472-18477. http://dx.doi.org/10.1073/pnas.1418545112

Elshorbany Y. F., Steil B., Brühl C., & Lelieveld J. (2012). Impact of HONO on global atmospheric chemistry calculated with an empirical parameterization in the EMAC model. *Atmospheric Chemistry and Physics*, *12*, 9977-10000. https://doi.org/10.5194/acp-12-9977-2012

Finlayson-Pitts B. J., Wingen L. M., Sumner A. L., Syomin D., & Ramazan K. A. (2003). The heterogeneous hydrolysis of NO_2 in laboratory systems and in outdoor and indoor atmospheres: An integrated mechanism. *Physical Chemistry Chemical Physics*, *5*, 223-242. https://doi.org/10.1039/B208564J

Ganzeveld L. N., Lelieveld J., Dentener F. J., Krol M. C., Bouwman A. J., & Roelofs G.-J. (2002). Global soil-biogenic NO_x emissions and the role of canopy processes. *Journal of Geophysical Research: Atmospheres*, *107*, ACH 9-1-ACH 9-17. https://doi.org/10.1029/2001JD001289

Gong P., Liu H., Zhang M., Li C., Wang J., Huang H., Clinton N., Ji L., Li W., Bai Y., Chen B., Xu B., Zhu Z., Yuan C., Ping Suen H., Guo J., Xu N., Li W., Zhao Y., Yang J., Yu C., Wang X., Fu H., Yu L., Dronova I., Hui F., Cheng X., Shi X., Xiao F., Liu Q., & Song L. (2019). Stable classification with limited sample: transferring a 30-m resolution sample set collected in 2015 to mapping 10-m resolution global land cover in 2017. *Science Bulletin*, *64*, 370-373. https://doi.org/10.1016/j.scib.2019.03.002

Gruber N., & Galloway J. N. (2008). An Earth-system perspective of the global nitrogen cycle. *Nature*, *451*, 293-296. https://doi.org/10.1038/nature06592

Homyak P. M., Vasquez K. T., Sickman J. O., Parker D. R., & Schimel J. P. (2015). Improving nitrite analysis in soils: drawbacks of the conventional 2 M KCl extraction. *Soil Science Society of America Journal*, *79*, 1237-1242. https://doi.org/10.2136/sssaj2015.02.0061n

Huang G., Zhou X., Deng G., Qiao H., & Civerolo K. (2002). Measurements of atmospheric nitrous acid and nitric acid. *Atmospheric Environment*, *36*, 2225-2235. https://doi.org/10.1016/S1352-2310(02)00170-X

Hudman R. C., Moore N. E., Mebust A. K., Martin R. V., Russell A. R., Valin L. C., & Cohen R. C. (2012). Steps towards a mechanistic model of global soil nitric oxide emissions: implementation and space based-constraints. *Atmospheric Chemistry and Physics*, *12*, 7779-7795. https://doi.org/10.5194/acp-12-7779-2012

Huffman G. J., Stocker E. F., Bolvin D. T., Nelkin E. J., & Tan J. (2019). GPM IMERG Late Precipitation L3 1 day 0.1 degree x 0.1 degree V06. In: Savtchenko A., & Greenbelt M., editors. Goddard Earth Sciences Data and Information Services Center (GES DISC), pp. 10.5067/GPM/IMERGDL/DAY/06.

Kim M., & Or D. (2019). Microscale pH variations during drying of soils and desert biocrusts affect HONO and NH_3 emissions. *Nature Communications*, *10*, 3944. https://doi.org/10.1038/s41467-019-11956-6

Laufs S., Cazaunau M., Stella P., Kurtenbach R., Cellier P., Mellouki A., Loubet B., & Kleffmann J. (2017). Diurnal fluxes of HONO above a crop rotation. *Atmospheric Chemistry and Physics*, *17*, 6907-6923. https://doi.org/10.5194/acp-17-6907-2017

Li G., Lei W., Zavala M., Volkamer R., Dusanter S., Stevens P., & Molina L. T. (2010). Impacts of HONO sources on the photochemistry in Mexico City during the MCMA-2006/MILAGO Campaign. *Atmospheric Chemistry and Physics*, *10*, 6551-6567. https://doi.org/10.5194/acp-10-6551-2010

Li K., Jacob D. J., Liao H., Shen L., Zhang Q., & Bates K. H. (2019). Anthropogenic drivers of 2013–2017 trends in summer surface ozone in China. *Proceedings of the National Academy of Sciences*, *116*, 422-427. https://doi.org/10.1073/pnas.1812168116

Li M., Zhang Q., Kurokawa J. I., Woo J. H., He K., Lu Z., Ohara T., Song Y., Streets D. G., Carmichael G. R., Cheng Y., Hong C., Huo H., Jiang X., Kang S., Liu F., Su H., & Zheng B. (2017). MIX: a mosaic Asian anthropogenic emission inventory under the international collaboration framework of the MICS-Asia and HTAP. *Atmospheric Chemistry and Physics*, *17*, 935-963. https://doi.org/10.5194/acp-17-935-2017

Liang J., Horowitz L. W., Jacob D. J., Wang Y., Fiore A. M., Logan J. A., Gardner G. M., & Munger J. W. (1998). Seasonal budgets of reactive nitrogen species and ozone over the United States, and export fluxes to the global atmosphere. *Journal of Geophysical Research: Atmospheres*, *103*, 13435-13450. https://doi.org/10.1029/97JD03126

Lu C., & Tian H. (2017). Global nitrogen and phosphorus fertilizer use for agriculture production in the past half century: shifted hot spots and nutrient imbalance. *Earth Syst. Sci. Data*, *9*, 181-192. https://doi.org/10.5194/essd-9-181-2017

Maljanen M., Yli-Pirilä P., Hytönen J., Joutsensaari J., & Martikainen P. J. (2013). Acidic northern soils as sources of atmospheric nitrous acid (HONO). *Soil Biology and Biochemistry*, *67*, 94-97. http://dx.doi.org/10.1016/j.soilbio.2013.08.013

Meusel H., Tamm A., Kuhn U., Wu D., Leifke A. L., Fiedler S., Ruckteschler N., Yordanova P., Lang-Yona N., Pöhlker M., Lelieveld J., Hoffmann T., Pöschl U., Su H., Weber B., & Cheng Y. (2018). Emission of nitrous acid from soil and biological soil crusts represents an important source of HONO in the remote atmosphere in Cyprus. *Atmospheric Chemistry and Physics*, *18*, 799-813. https://doi.org/10.5194/acp-18-799-2018

Miyazaki K., Eskes H., Sudo K., Boersma K. F., Bowman K., & Kanaya Y. (2017). Decadal changes in global surface NO_x emissions from multi-constituent satellite data assimilation. *Atmospheric Chemistry and Physics*, *17*, 807-837. https://doi.org/10.5194/acp-17-807-2017

Muñoz Sabater J. (2019). ERA5-Land monthly averaged data from 1981 to present. Copernicus Climate Change Service (C3S) Climate Data Store (CDS), Accessed on <15-07-2021>. https://doi.org/10.24381/cds.68d2bb3

Oswald R., Behrendt T., Ermel M., Wu D., Su H., Cheng Y., Breuninger C., Moravek A., Mougin E., Delon C., Loubet B., Pommerening-Röser A., Sörgel M., Pöschl U., Hoffmann T., Andreae M. O., Meixner F. X., & Trebs I. (2013). HONO emissions from soil bacteria as a major source of atmospheric reactive nitrogen. *Science*, *341*, 1233-1235. https://doi.org/10.1126/science.1242266

Pinder R. W., Davidson E. A., Goodale C. L., Greaver T. L., Herrick J. D., & Liu L. (2012). Climate change impacts of US reactive nitrogen. *Proceedings of the National Academy of Sciences*, *109*, 7671-5. https://doi.org/10.1073/pnas.1114243109

Plake D., Stella P., Moravek A., Mayer J. C., Ammann C., Held A., & Trebs I. (2015). Comparison of ozone deposition measured with the dynamic chamber and the eddy covariance method. *Agricultural and Forest Meteorology*, *206*, 97-112. https://doi.org/10.1016/j.agrformet.2015.02.014

Porada P., Tamm A., Raggio J., Cheng Y., Kleidon A., Pöschl U., & Weber B. (2019). Global NO and HONO emissions of biological soil crusts estimated by a process-based non-vascular vegetation model. *Biogeosciences*, *16*, 2003-2031. https://doi.org/10.1016/10.5194/bg-16-2003-2019

Ramsay R., Di Marco C. F., Heal M. R., Twigg M. M., Cowan N., Jones M. R., Leeson S. R., Bloss W. J., Kramer L. J., Crilley L., Sörgel M., Andreae M., & Nemitz E. (2018). Surface–atmosphere exchange of inorganic water-soluble gases and associated ions in bulk aerosol above agricultural grassland pre- and postfertilisation. *Atmospheric Chemistry and Physics*, *18*, 16953-16978. https://doi.org/10.5194/acp-18-16953-2018

Rasool Q. Z., Bash J. O., & Cohan D. S. (2019). Mechanistic representation of soil nitrogen emissions in the Community Multiscale Air Quality (CMAQ) model v 5.1. *Geosci. Model Dev.*, *12*, 849-878. https://doi.org/10.5194/gmd-12-849-2019

Ren X., Sanders J. E., Rajendran A., Weber R. J., Goldstein A. H., Pusede S. E., Browne E. C., Min K. E., & Cohen R. C. (2011). A relaxed eddy accumulation system for measuring vertical fluxes of nitrous acid. *Atmospheric Measurement Techniques*, *4*, 2093-2103. https://doi.org/10.5194/amt-4-2093-2011

Rummel, U., Ammann, C., Gut, A., Meixner, F. X., & Andreae M. O. (2002). Eddy covariance measurements of nitric oxide flux within an Amazonian rain forest. *Journal of Geophysical Research: Atmospheres*, *107*, LBA 17-1-LBA 17-9. https://doi.org/10.1029/2001JD000520

Scharko N. K., Schütte U. M. E., Berke A. E., Banina L., Peel H. R., Donaldson M. A., Hemmerich C., White J. R., & Raff J. D. (2015). Combined flux chamber and genomics approach links nitrous acid emissions to ammonia oxidizing bacteria and archaea in urban and agricultural soil. *Environmental Science & Technology*, *49*, 13825-13834. https://doi.org/10.1021/acs.est.5b00838

Shangguan W., Dai Y., Duan Q., Liu B., & Yuan H. (2014). A global soil data set for earth system modeling. *Journal of Advances in Modeling Earth Systems*, *6*, 249-263. https://doi.org/10.1002/2013MS000293

Sörgel M., Trebs I., Wu D., & Held A. (2015). A comparison of measured HONO uptake and release with calculated source strengths in a heterogeneous forest environment. *Atmospheric Chemistry and Physics*, *15*, 9237-9251. https://doi.org/10.5194/acp-15-9237-2015

Steinkamp J., & Lawrence M. G. (2011). Improvement and evaluation of simulated global biogenic soil NO emissions in an AC-GCM. *Atmospheric Chemistry and Physics*, *11*, 6063-6082. https://doi.org/10.5194/acp-11-6063-2011

Su H., Cheng Y., Oswald R., Behrendt T., Trebs I., Meixner F. X., Andreae M. O., Cheng P., Zhang Y., & Pöschl U. (2011). Soil nitrite as a source of atmospheric HONO and OH radicals. *Science*, *333*, 1616-1618. https://doi.org/10.1126/science.1207687

Tang K., Qin M., Duan J., Fang W., Meng F., Liang S., Xie P., Liu J., Liu W., Xue C., & Mu Y. (2019). A dual dynamic chamber system based on IBBCEAS for measuring fluxes of nitrous acid in agricultural fields in the North China Plain. *Atmospheric Environment*, *196*, 10-19. https://doi.org/10.1016/j.atmosenv.2018.09.059

Tang K., Qin M., Fang W., Duan J., Meng F., Ye K., Zhang H., Xie P., He Y., Xu W., Liu J., & Liu W. (2020). Simultaneous detection of atmospheric HONO and NO_2 utilising an IBBCEAS system based on an iterative algorithm. *Atmos. Meas. Tech.*, *13*, 6487-6499. https://doi.org/10.5194/amt-13-6487-2020

van Dijk S. M., Gut A., Kirkman G. A., Meixner F. X., Andreae M. O., & Gomes B. M. (2002). Biogenic NO emissions from forest and pasture soils: Relating laboratory studies to field measurements. *Journal of Geophysical Research*, *107*. https://doi.org/10.1029/2001jd000358

VandenBoer T. C., Young C. J., Talukdar R. K., Markovic M. Z., Brown S. S., Roberts J. M., & Murphy J. G. (2015). Nocturnal loss and daytime source of nitrous acid through reactive uptake and displacement. *Nature Geoscience*, *8*, 55-60. https://doi.org/10.1038/ngeo2298

Vinken G. C. M., Boersma K. F., Maasakkers J. D., Adon M., & Martin R. V. (2014). Worldwide biogenic soil NO_x emissions inferred from OMI NO_2 observations. *Atmospheric Chemistry and Physics*, *14*, 10363-10381. https://doi.org/10.5194/acp-14-10363-2014

Wang Q., Zhou F., Shang Z., Ciais P., Winiwarter W., Jackson R. B., Tubiello F. N., Janssens-Maenhout G., Tian H., Cui X., Canadell J. G., Piao S., & Tao S. (2019). Data-driven estimates of global nitrous oxide emissions from croplands. *National Science Review*, *7*, 441-452. https://doi.org/10.1093/nsr/nwz087

Wang Y., Fu X., Wu D., Wang M., Lu K., Mu Y., Liu Z., Zhang Y., & Wang T. (2021). Agricultural fertilization aggravates air pollution by stimulating soil nitrous acid emissions at high soil moisture. *Environmental Science & Technology*, *55*, 14556-14566. https://doi.org/10.1021/acs.est.1c04134

Weber B., Wu D., Tamm A., Ruckteschler N., Rodríguez-Caballero E., Steinkamp J., Meusel H., Elbert W., Behrendt T., Sörgel M., Cheng Y., Crutzen P. J., Su H., & Pöschl U. (2015). Biological soil crusts accelerate the nitrogen cycle through large NO and HONO emissions in drylands. *Proceedings of the National Academy of Sciences*, *112*, 15384-15389. https://doi.org/10.1073/pnas.1515818112

Winkler J. P., Cherry R. S., & Schlesinger W. H. (1996). The Q_{10} relationship of microbial respiration in a temperate forest soil. *Soil Biology and Biochemistry*, *28*, 1067-1072. https://doi.org/10.1016/0038-0717(96)00076-4

Wu D., Deng L., Liu Y., Xi D., Zou H., Wang R., Sha Z., Pan Y., Hou L., & Liu M. (2020). Comparisons of the effects of different drying methods on soil nitrogen fractions: Insights into emissions of reactive nitrogen gases (HONO and NO). *Atmospheric and Oceanic Science Letters*, *13*, 224-231. https://doi.org/10.1080/16742834.2020.1733388

Wu D., Horn M. A., Behrendt T., Müller S., Li J., Cole J. A., Xie B., Ju X., Li G., Ermel M., Oswald R., Fröhlich-Nowoisky J., Hoor P., Hu C., Liu M., Andreae M. O., Pöschl U., Cheng Y., Su H., Trebs I., Weber B., & Sörgel M. (2019). Soil HONO emissions at high moisture content are driven by microbial nitrate reduction to nitrite: tackling the HONO puzzle. *The ISME Journal*, *13*, 1688-1699. https://doi.org/10.1038/s41396-019-0379-y

Xu-Ri, & Prentice I. C. (2008). Terrestrial nitrogen cycle simulation with a dynamic global vegetation model. *Global Change Biology*, *14*, 1745-1764. https://doi.org/10.1111/j.1365-2486.2008.01625.x

Xue C., Ye C., Zhang C., Catoire V., Liu P., Gu R., Zhang J., Ma Z., Zhao X., Zhang W., Ren Y., Krysztofiak G., Tong S., Xue L., An J., Ge M., Mellouki A., & Mu Y. (2021). Evidence for strong HONO emission from fertilized agricultural fields and its remarkable impact on regional O_3 pollution in the summer North China Plain. *ACS Earth and Space Chemistry*, *5*, 340-347. https://doi.org/10.1021/acsearthspacechem.0c00314

Xue C., Ye C., Zhang Y., Ma Z., Liu P., Zhang C., Zhao X., Liu J., & Mu Y. (2019). Development and application of a twin open-top chambers method to measure soil HONO emission in the North China Plain. *Science of the Total Environment*, *659*, 621-631. https://doi.org/10.1016/j.scitotenv.2018.12.245

Yan X., Ohara T., & Akimoto H. (2005). Statistical modeling of global soil NO_x emissions. *Global Biogeochemical Cycles*, *19*, GB3019. https://doi.org/10.1029/2004GB002276

Yienger J. J., & Levy II H. (1995). Empirical model of global soil-biogenic NO_x emissions. *Journal of Geophysical Research: Atmospheres*, *100*, 11447-11464. https://doi.org/10.1029/95JD00370

Zhang J., An J., Qu Y., Liu X., & Chen Y. (2019). Impacts of potential HONO sources on the concentrations of oxidants and secondary organic aerosols in the Beijing-Tianjin-Hebei region of China. *Science of the Total Environment*, *647*, 836-852. https://doi.org/10.1016/j.scitotenv.2018.08.030

Zhang L., Wang T., Zhang Q., Zheng J., Xu Z., & Lv M. (2016). Potential sources of nitrous acid (HONO) and their impacts on ozone: A WRF-Chem study in a polluted subtropical region. *Journal of Geophysical Research: Atmospheres*, *121*, 3645-3662. https://doi.org/10.1002/2015JD024468

Zheng B., Tong D., Li M., Liu F., Hong C., Geng G., Li H., Li X., Peng L., Qi J., Yan L., Zhang Y., Zhao H., Zheng Y., He K., & Zhang Q. (2018). Trends in China's anthropogenic emissions since 2010 as the consequence of clean air actions. *Atmospheric Chemistry and Physics*, *18*, 14095-14111. https://doi.org/10.5194/acp-18-14095-2018

Zhu Z., Bi J., Pan Y., Ganguly S., Anav A., Xu L., Samanta A., Piao S., Nemani R. R., & Myneni R. B. (2013). Global data sets of vegetation leaf area index (LAI)3g and fraction of photosynthetically active radiation (FPAR)3g derived from Global Inventory Modeling and Mapping Studies (GIMMS) normalized difference vegetation index (NDVI3g) for the period 1981 to 2011. *Remote Sensing*, *5*, 927-948. https://doi.org/10.3390/rs5020927

References from the Supporting Information

Bhattarai H. R., Liimatainen M., Nykänen H., Kivimäenpää M., Martikainen P. J., & Maljanen M. (2019). Germinating wheat promotes the emission of atmospherically significant nitrous acid (HONO) gas from soils. *Soil Biology and Biochemistry*, *136*, 107518. https://doi.org/10.1016/j.soilbio.2019.06.014

Crippa M., Guizzardi D., Muntean M., Schaaf E., Dentener F., van Aardenne J. A., Monni S., Doering U., Olivier J. G. J., Pagliari V., & Janssens-Maenhout G. (2018). Gridded emissions of air pollutants for the period 1970–2012 within EDGAR v4.3.2. *Earth System Science Data*, *10*, 1987-2013. https://doi.org/10.5194/essd-10-1987-2018

Gu B., Ju X., Chang J., Ge Y., & Vitousek P. M. (2015). Integrated reactive nitrogen budgets and future trends in China. *Proceedings of the National Academy of Sciences*, *112*, 8792-8797. https://doi.org/10.1073/pnas.1510211112

Hickman J. E., Huang Y., Wu S., Diru W., Groffman P. M., Tully K. L., & Palm C. A. (2017). Nonlinear response of nitric oxide fluxes to fertilizer inputs and the impacts of agricultural intensification on tropospheric ozone pollution in Kenya. *Global Change Biology*, *23*, 3193-3204. https://doi.org/10.1111/gcb.13644

Huang Y., & Li D. (2014). Soil nitric oxide emissions from terrestrial ecosystems in China: a synthesis of modeling and measurements. *Scientific Reports*, *4*, 7406. https://doi.org/10.1038/srep07406

Li L., Chen C. H., Huang C., Huang H. Y., Zhang G. F., Wang Y. J., Wang H. L., Lou S. R., Qiao L. P., Zhou M., Chen M. H., Chen Y. R., Streets D. G., Fu J. S., & Jang C. J. (2012). Process analysis of regional ozone formation over the Yangtze River Delta, China using the Community Multi-scale Air Quality modeling system. *Atmospheric Chemistry and Physics*, *12*, 10971-10987. https://doi.org/10.5194/acp-12-10971-2012

Lin J. T. (2012). Satellite constraint for emissions of nitrogen oxides from anthropogenic, lightning and soil sources over East China on a high-resolution grid. *Atmospheric Chemistry and Physics*, *12*, 2881-2898. https://doi.org/10.5194/acp-12-2881-2012

Lin Y.-L., Farley R. D., & Orville H. D. (1983). Bulk Parameterization of the Snow Field in a Cloud Model. *Journal of Applied Meteorology and Climatology*, *22*, 1065-1092. https://doi.org/10.1175/1520-0450(1983)022<1065:Bpotsf>2.0.Co;2

Liu S., Lin F., Wu S., Ji C., Sun Y., Jin Y., Li S., Li Z., & Zou J. (2017). A meta-analysis of fertilizer-induced soil NO and combined NO+N_2O emissions. *Global Change Biology*, *23*, 2520-2532. https://doi.org/10.1111/gcb.13485

Mei B., Zheng X., Xie B., Dong H., Zhou Z., Wang R., Deng J., Cui F., Tong H., & Zhu J. (2009). Nitric oxide emissions from conventional vegetable fields in southeastern China. *Atmospheric Environment*, *43*, 2762-2769. https://doi.org/10.1016/j.atmosenv.2009.02.040

Mushinski R. M., Phillips R. P., Payne Z. C., Abney R. B., Jo I., Fei S., Pusede S. E., White J. R., Rusch D. B., & Raff J. D. (2019). Microbial mechanisms and ecosystem flux estimation for aerobic NO_y emissions from deciduous forest soils. *Proceedings of the National Academy of Sciences*, *116*, 2138-2145. https://doi.org/10.1073/pnas.1814632116

Palmer K., Drake H. L., & Horn M. A. (2010). Association of novel and highly diverse acid-tolerant denitrifiers with N_2O fluxes of an acidic fen. *Applied and Environmental Microbiology*, *76*, 1125-1134. https://doi.org/10.1128/AEM.02256-09

Pilegaard K. (2013). Processes regulating nitric oxide emissions from soils. *Philosophical Transactions of the Royal Society B: Biological Sciences*, *368*, 20130126. https://doi.org/10.1098/rstb.2013.0126

Ryan R. G., Rhodes S., Tully M., Wilson S., Jones N., Frieß U., & Schofield R. (2018). Daytime HONO, NO_2 and aerosol distributions from MAX-DOAS observations in Melbourne. *Atmospheric Chemistry and Physics*, *18*, 13969-13985. https://doi.org/10.5194/acp-18-13969-2018

Stutz J., Alicke B., & Neftel A. (2002). Nitrous acid formation in the urban atmosphere: Gradient measurements of NO_2 and HONO over grass in Milan, Italy. *Journal of Geophysical Research: Atmospheres*, *107*, 8192. https://doi.org/10.1029/2001JD000390

Tsai C., Spolaor M., Colosimo S. F., Pikelnaya O., Cheung R., Williams E., Gilman J. B., Lerner B. M., Zamora R. J., Warneke C., Roberts J. M., Ahmadov R., de Gouw J., Bates T., Quinn P. K., & Stutz J. (2018). Nitrous acid formation in a snow-free wintertime polluted rural area. *Atmospheric Chemistry and Physics*, *18*, 1977-1996. https://doi.org/10.5194/acp-18-1977-2018

Wang F., An J., Li Y., Tang Y., Lin J., Qu Y., Chen Y., Zhang B., & Zhai J. (2014). Impacts of uncertainty in AVOC emissions on the summer RO_x budget and ozone production rate in the three most rapidly-developing economic growth regions of China. *Advances in Atmospheric Sciences*, *31*, 1331-1342. https://doi.org/10.1007/s00376-014-3251-z

Wang Q. g., Han Z., & Higano Y. (2005). An inventory of nitric oxide emissions from soils in China. *Environmental Pollution*, *135*, 83-90. https://doi.org/10.1016/j.envpol.2004.10.007

Wang X., Zhang Y., Hu Y., Zhou W., Lu K., Zhong L., Zeng L., Shao M., Hu M., & Russell A. G. (2010). Process analysis and sensitivity study of regional ozone formation over the Pearl River Delta, China, during the PRIDE-PRD2004 campaign using the Community Multiscale Air Quality modeling system. *Atmospheric Chemistry and Physics*, *10*, 4423-4437. https://doi.org/10.5194/acp-10-4423-2010

Wong K. W., Tsai C., Lefer B., Haman C., Grossberg N., Brune W. H., Ren X., Luke W., & Stutz J. (2012). Daytime HONO vertical gradients during SHARP 2009 in Houston, TX. *Atmospheric Chemistry and Physics*, *12*, 635-652. https://doi.org/10.5194/acp-12-635-2012

Wu D., Kampf C. J., Pöschl U., Oswald R., Cui J., Ermel M., Hu C., Trebs I., & Sörgel M. (2014). Novel tracer method to measure isotopic labeled gas-phase nitrous acid ($HO^{15}NO$) in biogeochemical studies. *Environmental Science & Technology*, *48*, 8021-8027. https://doi.org/10.1021/es501353x

Xu P., Chen A., Houlton B. Z., Zeng Z., Wei S., Zhao C., Lu H., Liao Y., Zheng Z., Luan S., & Zheng Y. (2020). Spatial variation of reactive nitrogen emissions from China's croplands codetermined by regional urbanization

and its feedback to global climate change. *Geophysical Research Letters*, *47*, e2019GL086551. https://doi.org/10.1029/2019GL086551

Zhang H., Li J., Ying Q., Yu J. Z., Wu D., Cheng Y., He K., & Jiang J. (2012). Source apportionment of PM2.5 nitrate and sulfate in China using a source-oriented chemical transport model. *Atmospheric Environment*, *62*, 228-242. https://doi.org/10.1016/j.atmosenv.2012.08.014

Zhou X., Zhang N., TerAvest M., Tang D., Hou J., Bertman S., Alaghmand M., Shepson P. B., Carroll M. A., Griffith S., Dusanter S., & Stevens P. S. (2011). Nitric acid photolysis on forest canopy surface as a source for tropospheric nitrous acid. *Nature Geoscience*, *4*, 440-443. https://doi.org/10.1038/ngeo1164